Available online at www.sciencedirect.com

ScienceDirect

Underground Space 25 (2025) 350–367

www.keaipublishing.com/undsp

Research Paper

EDA-TCNet: A dual-attention enhanced network for precise point cloud segmentation in tunnel construction

Xin Peng, Mingnian Wang *, Bingxu Huang, Honglin Shen, Hao Zhong

State Key Laboratory of Intelligent Geotechnics and Tunnelling, Southwest Jiaotong University, Chengdu 610036, China

Received 19 December 2024; received in revised form 16 February 2025; accepted 15 April 2025
Available online 15 October 2025

Abstract

To enhance the accuracy of point cloud semantic segmentation in tunnel face construction areas, this study proposes a novel model named enhanced dual attention-tunnel construction net (EDA-TCNet). EDA-TCNet introduces a 3D enhanced dual attention module (EDAM), which employs a parallel channel and spatial attention mechanism to strengthen the model's focus on critical features. Additionally, a loss function named CELDAM is designed, combining cross-entropy loss and label-distribution-aware margin loss to effectively address data imbalance issues and improve the prediction capability for minority classes. Experiments conducted on three ongoing tunnel projects in Northwest China demonstrate that EDA-TCNet achieves a mean intersection over union (mIoU) of 0.8816 and an overall accuracy (OA) of 0.9406 on the test set. Compared to PointNet, PointNet++, DGCNN, and PointMLP, EDA-TCNet improves mIoU by 18.20%, 3.00%, 8.61%, and 32.23%, and OA by 15.98%, 1.74%, 5.48%, and 22.38%, respectively. Furthermore, the optimization of the balancing coefficient μ in CELDAM further enhances the model's generalization capability. In conclusion, EDA-TCNet demonstrates exceptional performance in point cloud semantic segmentation tasks for tunnel construction areas and shows great potential for engineering applications.

Keywords: Point cloud; Semantic segmentation; Deep learning; Enhanced dual attention; Tunnel construction

1 Introduction

China, with its extensive tunnel construction projects, is rightly regarded as a major global tunneling power. By the end of 2023, China had a total of 18 573 operational railway tunnels, spanning approximately 23 508 km (Gong et al., 2024). About two-thirds of China's land area consists of mountainous terrain (He & Wang, 2013), and these complex geographical conditions make mountain tunnel construction indispensable for improving transportation capacity. Mountain tunnel construction typically adopts tunnel boring machine (TBM) technology and the drilling-and-blasting method (Zhu et al., 2019). Compared to TBM, the drilling-and-blasting method, with its high adaptability and flexibility in complex geological conditions, is widely considered the preferred technique for mountain tunnel construction. During tunnel construction, ensuring safety and efficiency relies on the precise measurement of geological and deformation data. However, with changes in the labor force structure and the impact of an aging population, traditional manual measurement methods have gradually exposed significant drawbacks, including low work efficiency, labor shortages, and considerable safety risks (Zeng & Wang, 2014). Therefore, replacing manual operations with automated technologies has become an inevitable trend. Semantic segmentation technology provides critical support for achieving automated measurements, laying the foundation for advancements in this field.

The information from the tunnel face construction area is critically important, with each part serving specific key functions, including: (1) Revealing the geological charac-

* Corresponding author.
E-mail address: wmn00525@my.swjtu.edu.cn (M. Wang).
Peer review under the responsibility of Tongji University

https://doi.org/10.1016/j.undsp.2025.04.012

teristics of the tunnel face: The tunnel face directly reflects key geological characteristics of the rock mass (Barton, 1988), including the development and orientation of discontinuities, rock mass seepage, lithology, degree of weathering, and the presence of weak interlayers (Chen et al., 2020, 2021b; García-Luna et al., 2019; Monsalve et al., 2019; Peng et al., 2024). (2) Analysis of deformation and roughness in the initial support: Monitoring the deformation of the initial support is crucial for assessing the stability of the tunnel structure (Attard et al., 2018; Nuttens et al., 2014). Furthermore, the flatness of the initial support significantly impacts the durability of the tunnel lining (Fang et al., 2024). (3) Ground flatness analysis: The flatness of the ground is essential for the smooth operation of large construction machinery, serving as a key factor in ensuring construction efficiency and a prerequisite for achieving intelligent scheduling. (4) Blast effect analysis of the excavation profile: The excavation profile provides critical data for analyzing overbreak and underbreak analysis phenomena, helping to optimize blasting parameters, better control excavation results, and reduce construction costs (Daraei & Zare, 2018; Mahtab et al., 1997; Singh & Xavier, 2005).

Traditional manual measurement is a conventional method used during tunnel construction, with different measurement approaches applied to various construction segments. (1) Traditional geological investigation of the tunnel face. Typically, manual measurements adopt techniques recommended by the International Society for Rock Mechanics (ISRM) to assess geological conditions (Zhou et al., 2024). For instance, tape measures and survey lines are used to determine the spacing between discontinuities, while compasses are employed to measure their orientations (Battulwar et al., 2021; Kemeny & Post, 2003; Priest, 1993). This method requires close proximity to the rock mass and is highly subjective (Chen, Yang, et al., 2021; Gischig et al., 2011; Singh et al., 2021). (2) Overbreak and underbreak measurements of the excavation profile. Single-point measurements are conducted using total stations, but the number of measurement points is limited. (3) Deformation measurement of the initial support. Deformation monitoring relies on total stations, but the number of measurement points is minimal, primarily focusing on critical points such as deformation at the vault and settlement at the crown. The data collected are scattered, making it challenging to comprehensively capture the overall deformation of the support structure. (4) Measurement of ground flatness. Ground flatness is assessed visually, heavily relying on the expertise and experience of on-site personnel. In summary, traditional manual measurement methods in tunnel construction suffer from several drawbacks, including low efficiency, limited data collection, high subjectivity, and significant safety risks. Additionally, prolonged execution of multiple measurement tasks in tunnels may negatively impact the physical and mental health of survey personnel (Ji et al., 2023).

The advent of 3D point cloud technology has significantly advanced semi-automated measurement techniques in tunnel engineering, providing a more efficient and precise alternative to traditional measurement methods (Singh et al., 2023). The primary technologies for acquiring 3D point cloud data include radar, laser scanners, and photogrammetry (Drews et al., 2018). Among these, laser scanners are the ideal choice for point cloud acquisition in underground engineering due to their high precision, rapid data collection, and insensitivity to lighting conditions (Zhou et al., 2024). With continuous advancements in 3D point cloud technology, various research directions based on point cloud data have emerged. For instance, extensive studies have been conducted on algorithms for extracting and characterizing rock mass discontinuities (Peng et al., 2024; Singh et al., 2022). Additionally, the analysis of overbreak and underbreak in excavation profiles has become a research hotspot. By leveraging 3D point cloud data, excavation profile deviations can be accurately captured, enabling the optimization of blasting design parameters (Foderà et al., 2020; Hong et al., 2023). Moreover, studies focusing on initial support structures' deformation and surface roughness have also gained traction (Fang et al., 2024; Han et al., 2013; Nuttens et al., 2014; Roca-Pardiñas et al., 2014). Ground flatness analysis based on point cloud data has further expanded the application of this technology (Yang et al., 2023). As illustrated in Fig. 1, 3D point cloud data have been widely applied to measure various parts of the tunnel face construction area, driving innovation and precision in tunnel engineering.

Semantic segmentation plays a crucial role in the field of 3D point cloud processing, as it enables accurate identification and classification of various objects in complex scenes, thereby providing essential data support for subsequent engineering analysis and decision-making. PointNet, the first neural network specifically designed for point clouds, introduced a groundbreaking approach by directly processing unordered point sets, overcoming the limitations of traditional convolutional neural networks in handling 3D data (Qi et al., 2017a). By independently extracting features for each point and using symmetric functions to address the unordered nature of point clouds, PointNet achieved significant performance improvements on multiple benchmark datasets. However, PointNet faces limitations in capturing local structural information, particularly when processing point clouds with complex geometric shapes and intricate details. To address this issue, PointNet++ was developed (Qi et al., 2017b). By introducing a hierarchical feature extraction mechanism that progressively aggregates local region features, PointNet++ effectively captures the local geometric information of point clouds, significantly improving the accuracy and robustness of semantic segmentation. The success of the PointNet series has spurred widespread academic interest in point cloud semantic segmentation, leading to the emergence of numerous novel network architectures. For instance, DGCNN

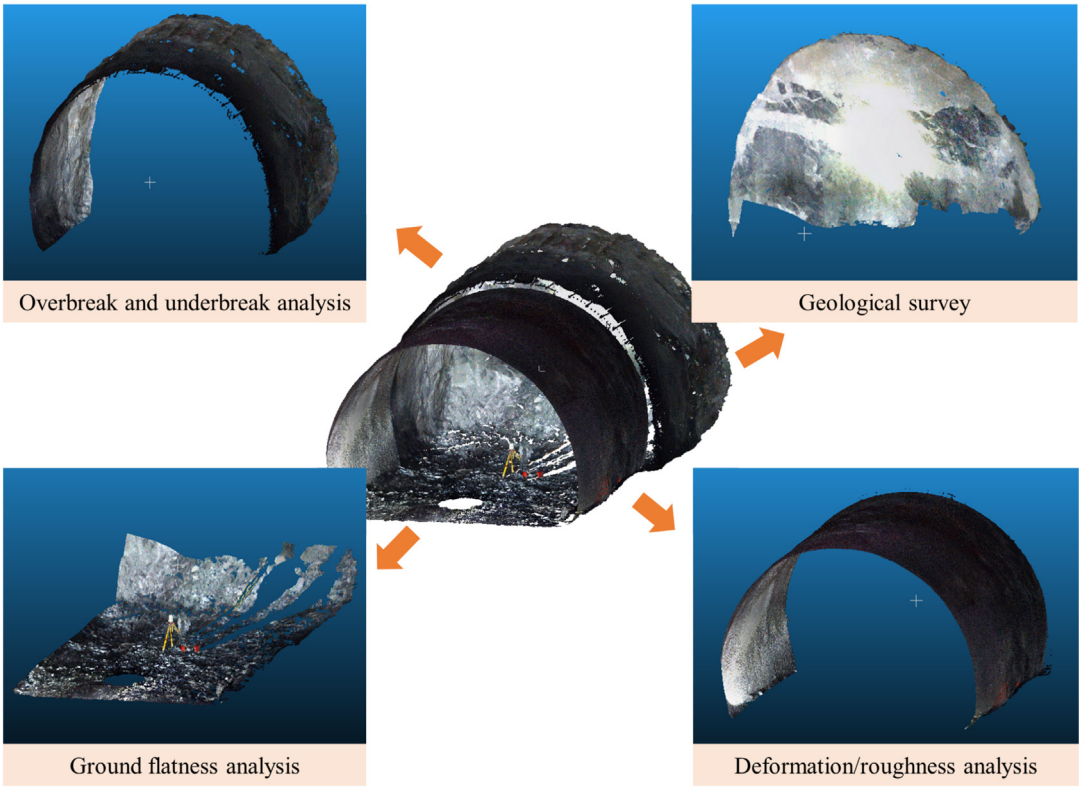

Fig. 1. Applications of 3D point cloud analysis in various sections of the tunnel face excavation area.

enhances the local feature representation of point clouds by incorporating dynamic graph convolution operations (Phan et al., 2018). PointCNN leverages learnable convolution kernels to effectively capture local structures (Li et al., 2018). SGPN utilizes graph neural networks for efficient point-level feature propagation, while PointSIFT introduces a rotation-invariant feature extraction module to improve model robustness (Jiang et al., 2018; Wang et al., 2018). Additionally, Point Transformer integrates self-attention mechanisms to further enhance the performance of point cloud processing (Zhao et al., 2021), and PointMLP is a pure multilayer perceptron-based model for point cloud processing, designed for efficiency and high accuracy without convolution or attention mechanisms (Ma et al., 2022). These innovative advancements not only enrich the technical framework of 3D point cloud semantic segmentation but also provide more efficient and precise tools for practical engineering applications.

Advancements in semantic segmentation technology have not only driven its own development but also facilitated its widespread application across various fields, including building information modeling (BIM) (Zhang et al., 2024), agriculture (Sun et al., 2024), geographic information science (Xie et al., 2020), medicine (Zhang & Wang, 2021), and industry (Yin et al., 2021). In the domain of transportation infrastructure, point cloud semantic segmentation has garnered increasing attention and applications. Specifically, in bridge inspection, this technology enables the identification of individual bridge components, aiding in structural health monitoring (Lee et al., 2021). In the coal mining industry, point cloud semantic segmentation is utilized to segment different components within transportation tunnels, enhancing the efficiency of tunnel management (Kang et al., 2023). In the railway sector, the technology is applied to segment railway environments and automatically identify railway infrastructure, effectively supporting the daily operations and maintenance of railways (Grandio et al., 2023, 2022; Soilán et al., 2020). Furthermore, in subway tunnel operations, point cloud semantic segmentation is used for monitoring shield tunnels in subway systems, significantly improving the automation level of tunnel inspections (Cui et al., 2024; Ji et al., 2023; Lin et al., 2024; Zhang et al., 2022, 2023; Zhou et al., 2023). These diverse applications highlight the transformative potential of semantic segmentation in advancing efficiency and precision across various industries.

Despite the promising application prospects of point cloud segmentation technology in tunnel engineering, current research faces two major challenges. First, existing studies predominantly focus on the operational phase of tunnels, with limited attention to applications during the construction phase. This is in stark contrast to the pressing need for high-precision measurements during tunnel construction. Second, most research has been concentrated on shield subway tunnels, while studies targeting mountain tunnels constructed using the drilling-and-blasting method remain relatively scarce. Therefore, to address the practical

requirements of automated measurements during the construction phase of drilling-and-blasting mountain tunnels, it is imperative to conduct dedicated research on point cloud semantic segmentation tailored to construction-stage applications.

To improve the accuracy of point cloud semantic segmentation in tunnel face construction areas, this study proposes a novel segmentation model named enhanced dual attention-tunnel construction net (EDA-TCNet). First, a module called the 3D enhanced dual attention module (EDAM) is designed to enhance the model's ability to focus on critical features from both channel and spatial dimensions. Based on the EDAM module, an enhanced set abstraction layer (ESA) and an enhanced feature propagation layer (EFP) are constructed to further optimize feature extraction and propagation processes. Additionally, a novel loss function named cross-entropy with label-distribution-aware margin loss (CELDAM) is proposed to address issues caused by imbalanced data distribution, thereby improving the model's predictive performance for minority classes. The EDA-TCNet was then applied to real-world projects involving three ongoing tunnel construction sites in Northwest China. Comprehensive evaluations using metrics such as mean Intersection over Union (mIoU), overall accuracy (OA), Recall, and Precision, along with comparative analyses against classical models like PointNet, PointNet++, and DGCNN, were conducted to assess the model's segmentation accuracy. Finally, in the discussion section, the impact of the balancing coefficient μ in CELDAM on the model's performance is thoroughly analyzed.

2 Data collection

To enhance data diversity and adaptability while providing a robust foundation for subsequent research, this study conducted data collection across multiple tunnels. As shown in Fig. 2, systematic point cloud data acquisition was performed in three ongoing tunnel construction sites—Tunnel A, Tunnel B, and Tunnel C—located in Northwest China. During the data collection process, detailed records of lithological characteristics, geological conditions, and excavation conditions were maintained for each cycle to ensure data completeness and reliability.

As shown in Table 1, the collected data covers three distinct lithologies: trondhjemite from Tunnel A, fine-grained monzonitic granite from Tunnel B, and gneiss from Tunnel C. These lithologies exhibit varying degrees of weathering, ranging from slightly weathered to weakly weathered, and rock mass integrity that spans from moderately fractured to intact. In terms of functional classification, the data include two types of tunnels: Tunnel A and Tunnel B represent main tunnel sections, while Tunnel C serves as an auxiliary tunnel.

Figure 3 shows the process of point cloud data collection on-site, which includes placing the scanner, initiating the tablet operating system, remotely controlling the scanner, exporting point cloud files, cropping key regions, converting formats, and saving the data locally. The data collection spanned 22 days, covering 10, 14, and 5 cycles for Tunnels A, B, and C, respectively, with corresponding lengths of 32, 45, and 17 m, resulting in a total scanned length of 94 m. After preprocessing steps such as denoising

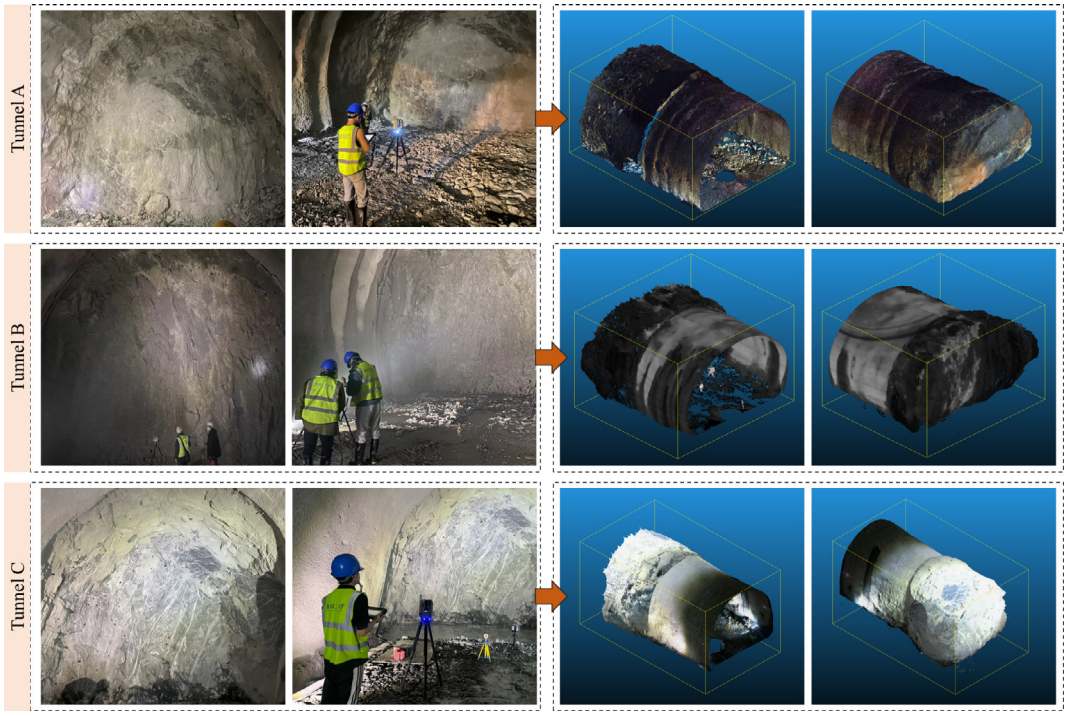

Fig. 2. Systematic point cloud data acquisition and geological condition recording from multiple tunnel construction sites.

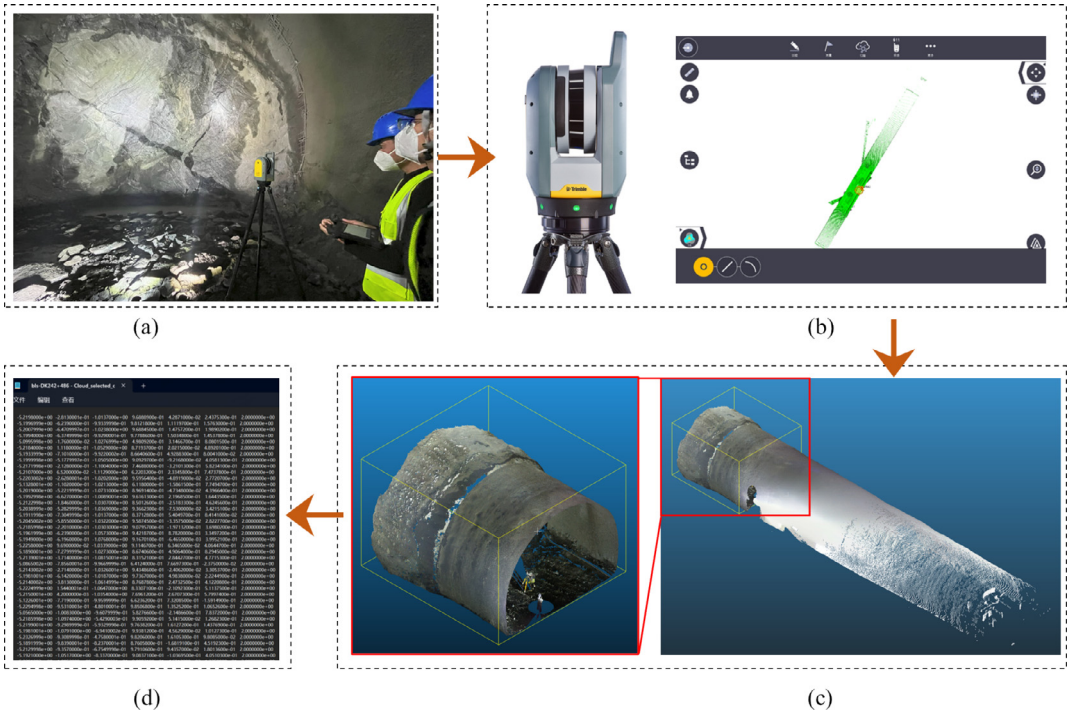

Fig. 3. Workflow of point cloud data acquisition and preprocessing in tunnel construction areas. (a) Project site, (b) scanner used, (c) the obtained point cloud, and (d) point cloud in txt format.

Table 1
Geological and functional characteristics of the surveyed tunnel sections.

Project	Lithology	Degree of weathering	Rock mass integrity	Functional type	Excavation area (m^2)
Tunnel A	Trondhjemite	Slightly weathered	Moderately fractured	Main tunnel section	119
Tunnel B	Fine-grained monzonitic granite	Moderately weathered	Moderately fractured	Main tunnel section	137
Tunnel C	Gneiss	Weakly weathered	Intact	Auxiliary tunnel	55

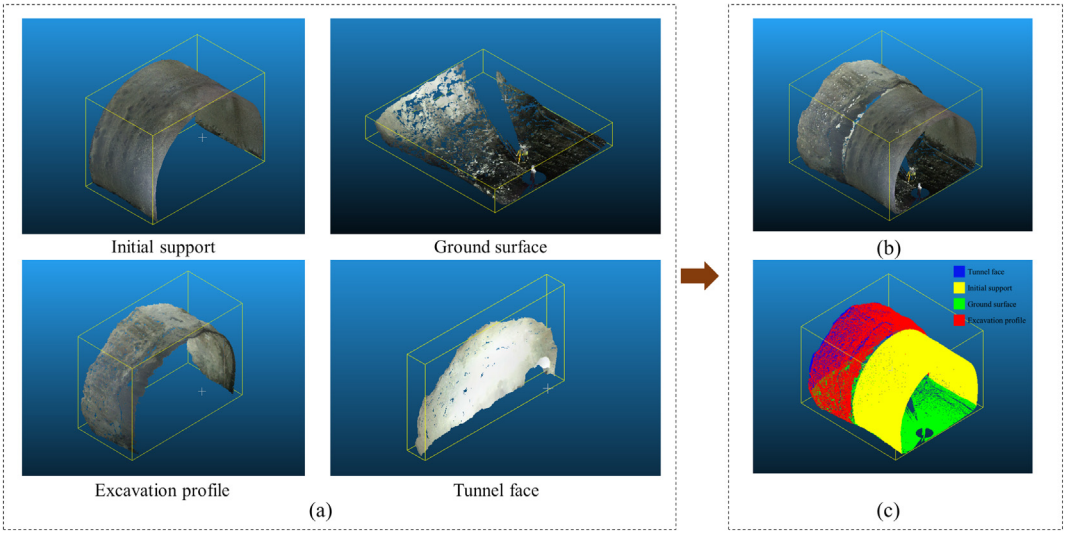

Fig. 4. Point cloud segmentation and labeling process. (a) Different parts of a point cloud, (b) original point cloud, and (c) labeled point cloud.

Table 2
Point cloud data distribution across the training, validation, and testing sets.

Set type	Tunnel face	Ground surface	Initial support	Excavation profile	Total
Training set	5 380 073	7 867 053	20 847 951	9 151 684	43 246 761
Validation set	2 227 406	2 670 133	7 074 216	2 897 903	14 869 658
Testing set	1 073 870	1 254 658	2 391 695	1 784 438	6 504 661
Total number of points					64 621 080

and cropping, a point cloud dataset comprising 64 621 080 points for the tunnel construction areas was obtained.

To meet the practical requirements of on-site construction, we collaborated with geological survey experts from the design unit, technical personnel from the construction unit, and professors from research institutions to accurately label the point cloud dataset. As shown in Fig. 4, the tunnel face construction area was divided into four parts: tunnel face, ground surface, excavation profile, and initial support section. Subsequently, each part was labeled using the CloudCompare software.

The dataset was divided into training set, validation set, and testing set based on an approximate 7:1:1 ratio. Table 2 presents the distribution of point cloud data across these subsets. A total of 64 621 080 points were collected, with the training set containing 43 246 761 points (66.93%), the validation set containing 14 869 658 points (23.01%), and the testing set containing 6 504 661 points (10.06%). However, the dataset exhibits significant class imbalance. As shown in Fig. 5, among the categories, the initial support class dominates in sample size across all subsets, while the tunnel face and ground surface categories have relatively fewer samples. Notably, the tunnel face class constitutes the smallest proportion in all datasets. This imbalance presents a valuable opportunity to evaluate the effectiveness of the proposed loss function in addressing such challenges.

3 Methodology

As shown in Fig. 6, this study proposes a novel network model, EDA-TCNet, specifically designed for the task of

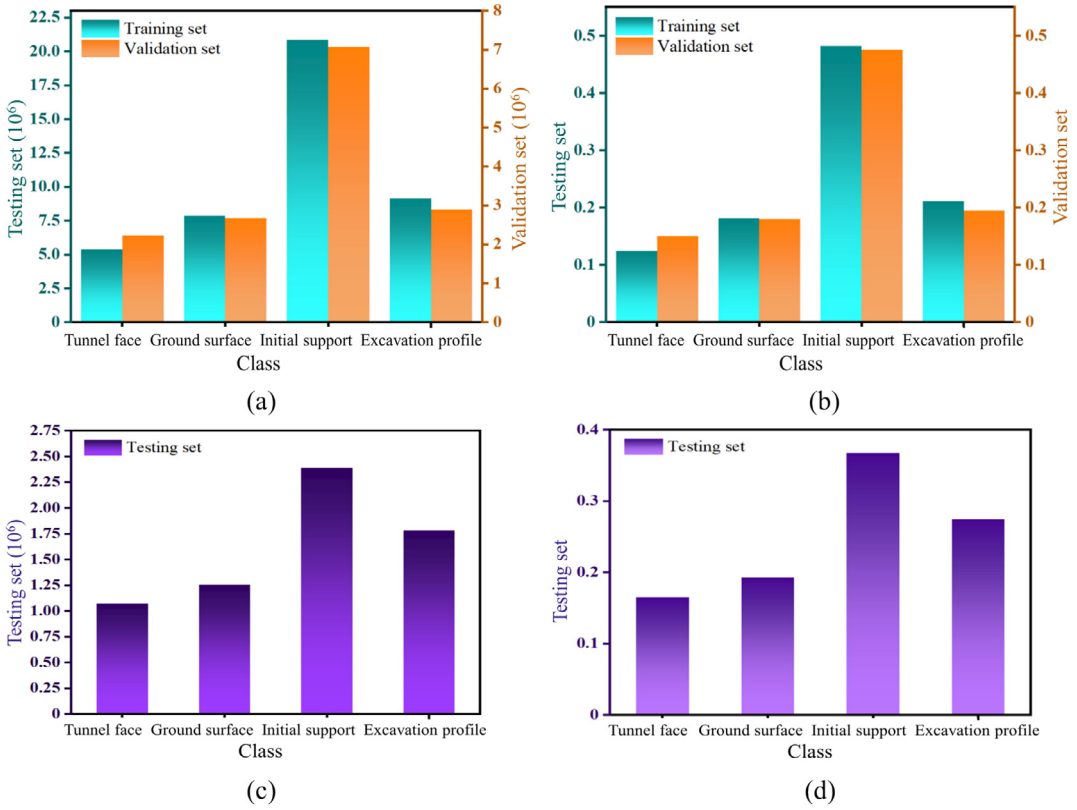

Fig. 5. Data distribution across classes in the training, validation, and testing sets. (a) Sample size—training & validation, (b) proportion—training & validation, (c) sample size—testing, and (d) proportion—testing.

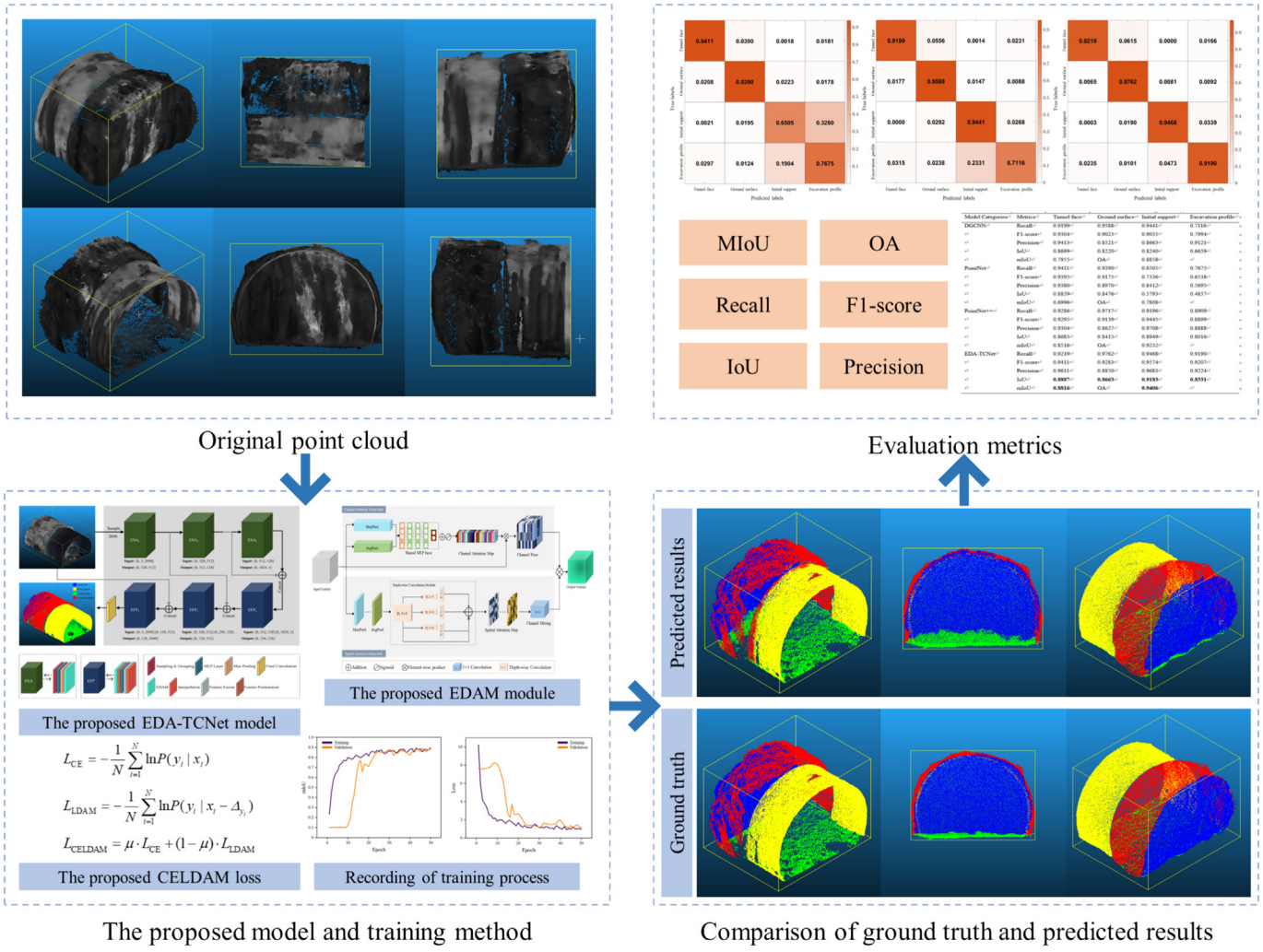

Fig. 6. Process flow of the proposed method.

point cloud semantic segmentation in tunnel construction areas. The overall framework comprises four key modules: data input, model design and training, qualitative visualization analysis, and comprehensive performance evaluation.

First, in the data input module, high-quality semantic datasets with multi-category information were generated through the acquisition, processing, and annotation of tunnel face point cloud data. These datasets provide a solid foundation for training and testing the proposed model. Second, in the model design and training module, the EDA-TCNet model was developed, incorporating a 3D EDAM to enhance feature extraction in complex scenarios. Additionally, a novel CELDAM Loss function was introduced to effectively address data imbalance issues. The optimization performance of the model was further validated by tracking the variations in loss functions and performance metrics during the training process. Third, in the qualitative visualization analysis module, the model's predictive performance across different regions was qualitatively evaluated by visually comparing ground truth with predicted results. Finally, in the comprehensive performance evaluation module, multiple metrics—including OA, mIoU, Recall, Precision, F_1-score, and IoU—were employed. In combination with confusion matrices and comparative experiments against traditional models, the performance of EDA-TCNet on the testing set was quantitatively assessed.

3.1 Proposed network structure

As shown in Fig. 7, we propose a model named EDA-TCNet, designed specifically for the task of point cloud semantic segmentation in tunnel construction areas. EDA-TCNet incorporates a novel 3D EDAM to enhance feature extraction and representation. The architecture of EDA-TCNet consists of three ESA layers and three EFP layers, enabling efficient extraction and integration of both local and global features within point cloud data. Moreover, the model leverages the 3D enhanced dual attention

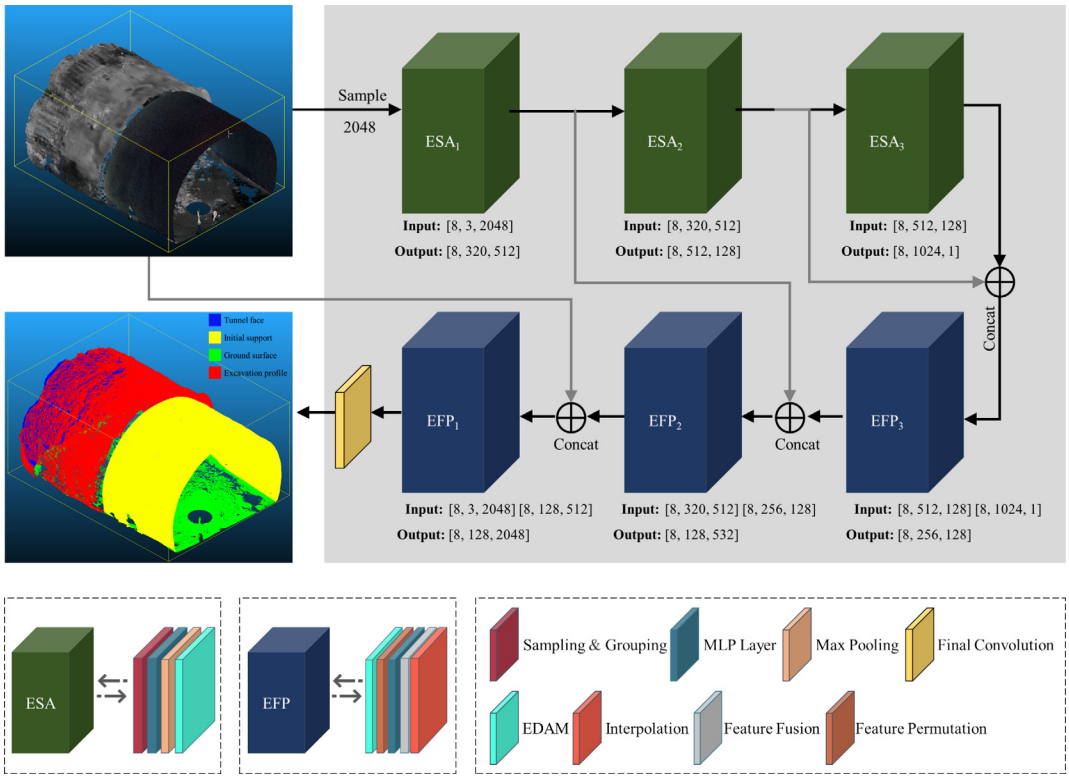

Fig. 7. Architecture of the proposed EDA-TCNet network.

mechanism to further improve the representation of critical features in key regions, ensuring more accurate segmentation.

The ESA layer primarily consists of a Sampling & Grouping layer, an MLP layer, a Max Pooling operation, and an EDAM module, designed to extract local and multi-scale spatial features from point cloud data. The role of the EDAM module within the ESA layer is to focus on critical regions of the point cloud, thereby enhancing the expression of local features. The EFP layer comprises an Interpolation layer, a Feature Fusion layer, a Max Pooling operation, a Feature Permutation layer, and an EDAM module, aimed at propagating high-level abstracted features back to lower levels for stepwise refinement. In the EFP layer, the EDAM module emphasizes critical contextual features, enhancing the feature refinement process and facilitating the recovery of global semantic information in the point cloud. By integrating multi-level feature extraction with the enhanced dual attention mechanism, the proposed EDA-TCNet is designed to improve the performance of point cloud semantic segmentation tasks in tunnel construction areas.

3.2 3D enhanced dual attention module

As shown in Fig. 8, this study introduces a novel 3D EDAM, which adopts a parallel attention mechanism to enhance feature representation by effectively combining channel attention and spatial attention. Unlike traditional serial attention mechanisms (e.g., the sequential structure of convolutional block attention module (CBAM) (Woo et al., 2018), 3D EDAM computes channel attention and spatial attention in parallel. This design allows the channel attention submodule to focus on "which features should be emphasized", while the spatial attention submodule simultaneously determines "where these features are distributed". By employing this parallel structure, 3D EDAM avoids the branch interference issue often encountered in serial mechanisms, achieving more efficient integration of channel and spatial information.

Additionally, to dynamically generate refined spatial attention maps, the spatial attention submodule in 3D EDAM incorporates a depth-wise convolution module. This module generates specific spatial attention distributions for each channel, enabling precise modeling of spatial relationships and capturing deeper correlations between local and global features. This design not only retains computational efficiency but also produces attention maps that closely align with the true feature distributions, further enhancing the accuracy of feature representation.

3.3 Performance metrics and loss function

This study introduces a specifically designed loss function named cross-entropy with label-distribution-aware margin loss (CELDAM, L_{CELDAM}) to address the class imbalance issue in point cloud semantic segmentation tasks for tunnel face construction areas. CELDAM combines the

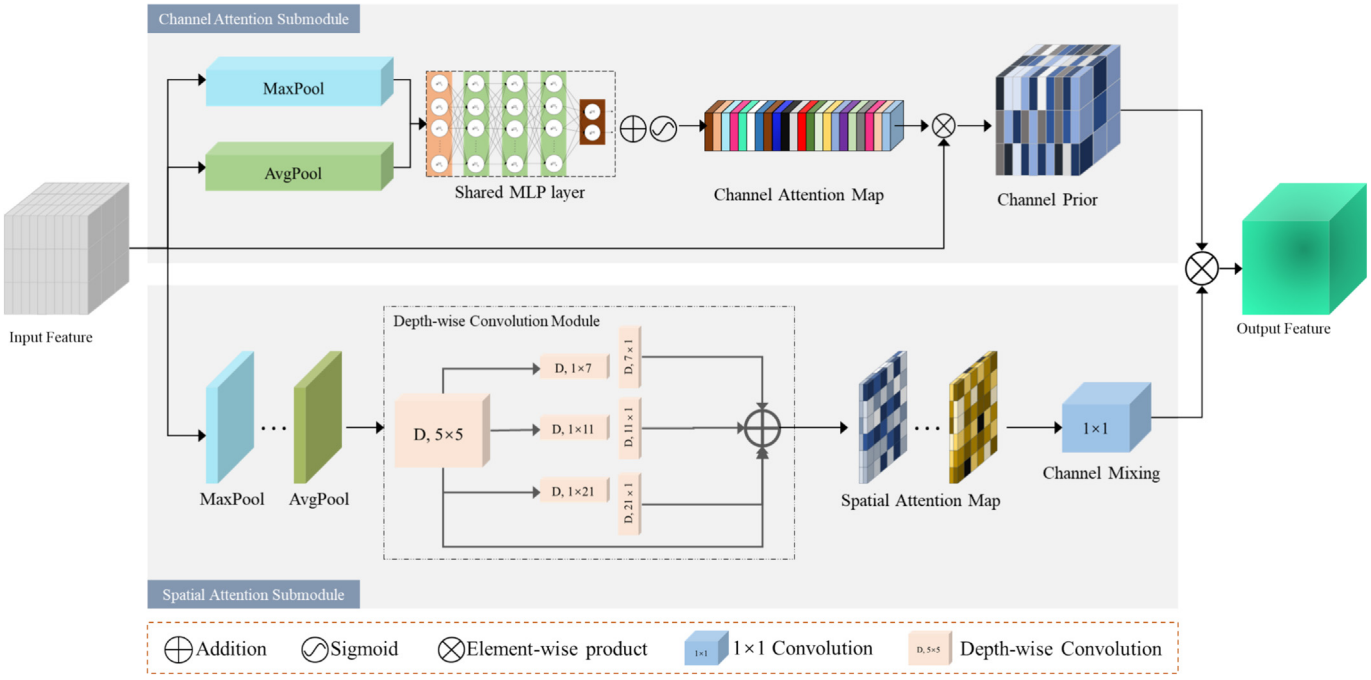

Fig. 8. Network architecture of the proposed 3D EDAM.

global classification capability of cross-entropy (CE) Loss with the class sensitivity of label-distribution-aware margin (LDAM) Loss. By integrating these two components, CELDAM enhances the model's learning ability for minority classes while maintaining overall classification performance. The definition of CELDAM is as follows:

$$L_{\mathrm{CELDAM}} = \mu \cdot L_{\mathrm{CE}} + (1-\mu) \cdot L_{\mathrm{LDAM}}, \tag{1}$$

where L_{CE} represents the standard Cross-Entropy Loss, and L_{LDAM} is the Label-Distribution-Aware Margin Loss. The parameter μ in CELDAM serves as a balancing coefficient to adjust the weight contributions of the two loss components.

As a foundational component of CELDAM, the CE Loss is a widely used loss function for classification tasks. Its primary objective is to maximize the predicted probability of the correct class, thereby enhancing the model's overall classification capability. For a given sample x_i and its corresponding target class y_i, the mathematical definition of CE Loss is

$$L_{\mathrm{CE}} = -\frac{1}{N}\sum_{i=1}^{N} \ln P(y_i|x_i), \tag{2}$$

where N represents the total number of samples, and $P(y_i|x_i)$ denotes the probability predicted by the model that sample x_i belongs to class y_i. CE Loss penalizes misclassified samples, compelling the model to learn global features for each class, thereby improving overall classification performance.

Another core component of CELDAM Loss is the LDAM Loss. The central idea of LDAM is to assign a margin adjustment term to each class based on its sample distribution. During optimization, this dynamically adjusted margin increases the penalty for misclassifications in minority classes, enhancing the model's learning focus on underrepresented categories. The mathematical definition of LDAM Loss is as follows:

$$L_{\mathrm{LDAM}} = -\frac{1}{N}\sum_{i=1}^{N} \ln P(y_i|x_i - \Delta_{y_i}), \tag{3}$$

where N is the total number of samples; $P(y_i|x_i - \Delta_{y_i})$ represents the predicted probability that the sample x_i belongs to category y_i after marginal adjustment; Δ_{y_i} is the marginal adjustment term for category y_i, defined as

$$\Delta_{y_i} = m_{y_i} \cdot \frac{1}{\sqrt{\sqrt{n_{y_i}}}}, \tag{4}$$

where n_{y_i} represents the number of samples of category y_i, and m_{y_i} is an adjustable maximum margin value that controls the magnitude of the margin adjustment.

In this study, a comprehensive set of metrics is employed to evaluate the performance of the model, including Recall, Precision, IoU, mIoU, OA, and F_1-score. Among these, Recall reflects the proportion of correctly identified samples of a specific class to the actual total number of samples in that class. Its definition is as follows:

$$\mathrm{Recall} = \frac{\mathrm{TP}}{\mathrm{TP} + \mathrm{FN}}, \tag{5}$$

where TP is the number of samples correctly classified into this category, and FN represents the number of samples that actually belong to this category but are not correctly classified.

Precision indicates the ratio of the number of samples correctly identified by the model to the total number of samples predicted by the model to be of that category. It is defined as follows:

$$\text{Precision} = \frac{\text{TP}}{\text{TP} + \text{FP}}, \tag{6}$$

where FP represents the number of samples that do not actually belong to this category but are misclassified as this category.

Intersection over Union (IoU) is used to measure the degree of overlap between the model prediction results and the true value, and is defined as follows:

$$\text{IoU} = \frac{\text{TP}}{\text{TP} + \text{FP} + \text{FN}}. \tag{7}$$

mIoU is the average value of IoU for all categories, which is used to measure the segmentation performance of the model for global data. It is defined as follows:

$$\text{mIoU} = \frac{1}{C}\sum_{i=1}^{C}\text{IoU}_i. \tag{8}$$

Among them, C represents the total number of categories, and IoU_i represents the IoU value of the i-th category.

OA indicates the ratio of the number of samples correctly classified by the model to the total number of samples, and is used to measure the overall classification performance of the model. It is defined as follows:

$$\text{OA} = \frac{\sum_{i=1}^{C}\text{TP}_i}{\sum_{i=1}^{C}(\text{TP}_i + \text{FP}_i + \text{FN}_i)}, \tag{9}$$

where TP_i is the number of correctly classified samples of the i-th category, and FP_i and FN_i represent the number of misclassified samples of the i-th category.

F_1-score is the harmonic average of Precision and Recall, which is used to comprehensively evaluate the accuracy and recall of the model. It is defined as follows:

$$F_1\text{-score} = \frac{2 \times \text{Precision} \times \text{Recall}}{\text{Precision} + \text{Recall}}. \tag{10}$$

4 Results of the experiments

4.1 Setup and details

The training environment was configured using the PyTorch 2.1 deep learning framework, running on a Windows operating system. GPU acceleration was achieved through CUDA 12.3, enhancing computational efficiency. During model training, 2048 points were processed per iteration, with the training spanning 50 epochs. The initial learning rate was set to 0.001 and adjusted using a step decay schedule to ensure stable convergence. The Adam optimizer was employed to optimize model parameters, and all experimental outcomes, including model weights and logs, were stored in a designated directory for detailed analysis and benchmarking.

The experiments were conducted on a Lenovo Legion Y7000P 2023 workstation, equipped with a 13th-generation Intel Core i7-13620H processor (2.40 GHz base frequency), 16 GB of RAM, and an NVIDIA GeForce RTX 4060 GPU. This hardware configuration provided sufficient computational capabilities and memory to process large-scale point cloud data and train deep learning models with high efficiency.

4.2 Evaluation of results

Figure 9 shows the trends of mIoU and loss across epochs on the training and validation sets. In Fig. 9(a), the mIoU curves show a significant upward trend during the early training stages (the first 20 epochs), indicating continuous learning and optimization by the model. Around the 22nd epoch, the validation mIoU begins to stabilize with slight fluctuations, suggesting that the model is nearing convergence. Meanwhile, the training mIoU continues to improve slightly and eventually reaches a peak value of 0.8966, with the training OA achieving a maximum of 0.9565. On the validation set, the mIoU fluctuates between the 20th and 50th epochs and ultimately achieves a best value of 0.8937, with the validation OA reaching a maximum of 0.9478. These metrics demonstrate the model's ability to effectively enhance its performance during training. In Fig. 9(b), the loss curves display a sharp decline in the early epochs, reflecting significant parameter adjustments in the initial stages of training. Around the 22nd epoch, the validation loss gradually stabilizes and aligns closely with the trend of the training loss in subsequent epochs. This alignment indicates that the training process is stable, and the model generalizes well to the validation data. Overall, the model demonstrates superior performance, achieving OA values exceeding 90% on both the training and validation sets. Additionally, the consistency between training and validation performance highlights the model's excellent generalization capability.

This study conducted a detailed comparison of the proposed EDA-TCNet model with four commonly used models (DGCNN, PointNet, PointNet++, and PointMLP) on both the training and validation sets. As shown in Table 3, EDA-TCNet demonstrates superior performance across all evaluation metrics. Specifically, on the validation set, it achieves the highest mIoU of 0.8937 and OA of 0.9478. Similarly, on the training set, EDA-TCNet attains the best mIoU of 0.8966 and OA of 0.9565. Compared to other models, the performance advantage of EDA-TCNet is particularly noteworthy, especially on the validation set, where it exhibits more stable and outstanding results.

The results show a pattern: although PointNet++ performs comparably to EDA-TCNet on the validation set, its performance drops significantly on the training set. In contrast, DGCNN, PointMLP, and PointNet exhibit noticeably lower mIoU and OA values than EDA-

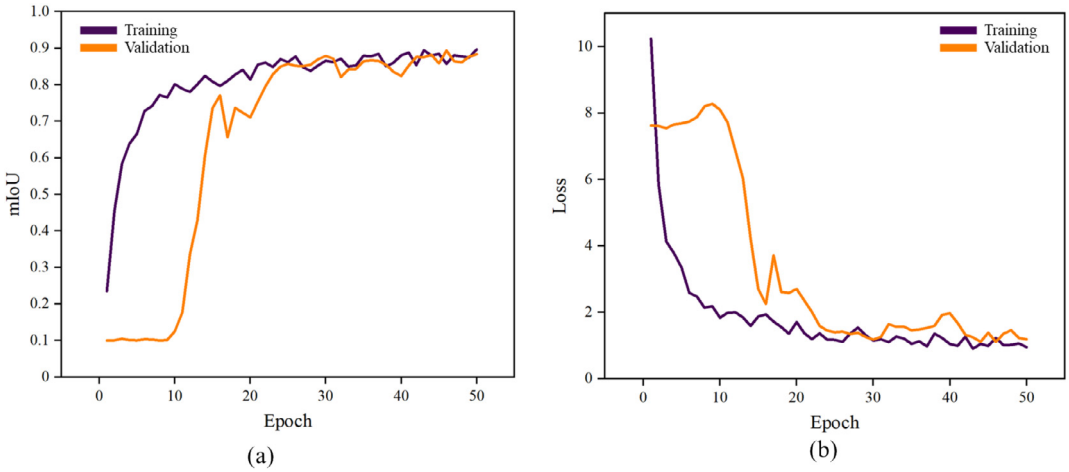

Fig. 9. (a) mIoU and (b) loss trends during training and validation.

Table 3
Comparison of model performance on training and validation sets.

Model categories	Validation		Training		Training time
	mIoU	OA	mIoU	OA	
DGCNN	0.8610	0.9310	0.8431	0.9340	35 min 59 s
PointNet	0.8511	0.9261	0.8414	0.9312	32 min 45 s
PointNet++	0.8602	0.9286	0.8907	0.9553	32 min 47 s
PointMLP	0.8707	0.9372	0.8716	0.9451	33 min 1 s
EDA-TCNet	**0.8937**	**0.9478**	**0.8966**	**0.9565**	32 min 51 s

TCNet, with their limitations particularly pronounced on the validation set. Overall, EDA-TCNet not only maintains high accuracy on the training set but also demonstrates superior generalization performance. Similarly, as summarized in Table 3 under the current experimental configuration, the training duration for all models ranges between 30 and 40 min.

To further evaluate the model's performance on the testing set, a visual comparison between the ground truth and predicted results was conducted, as shown in Figs. 10–12.

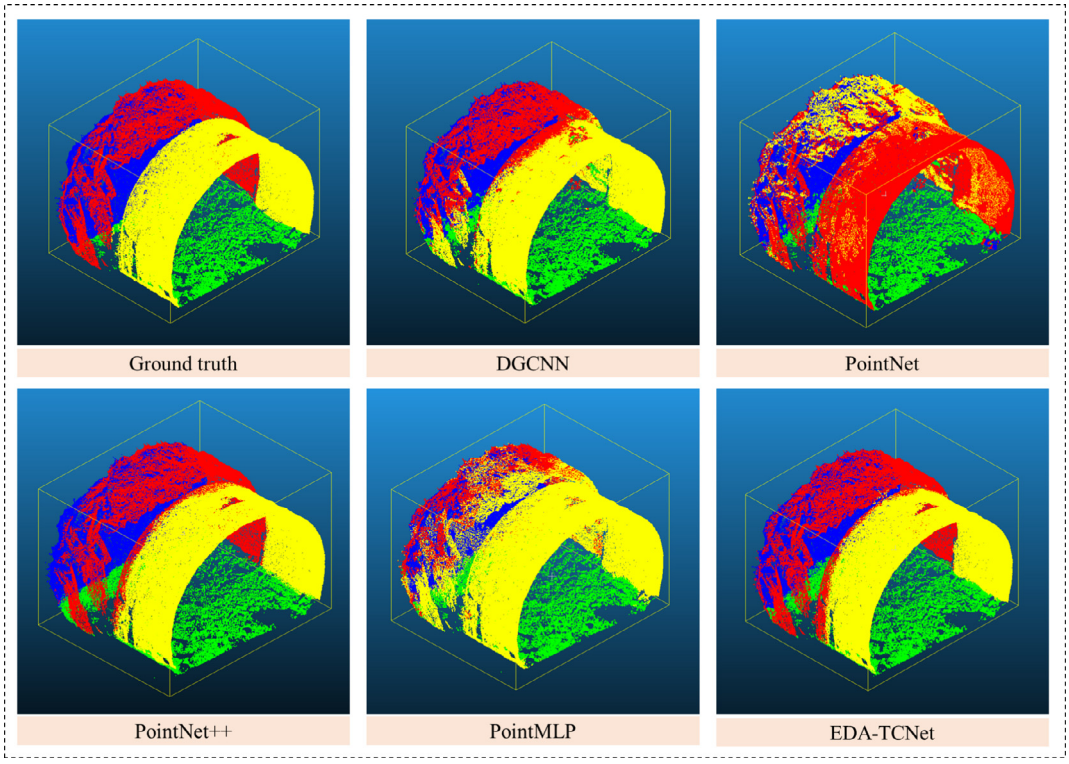

Fig. 10. Visual comparison between ground truth and predictions of the proposed model (front-side combined view).

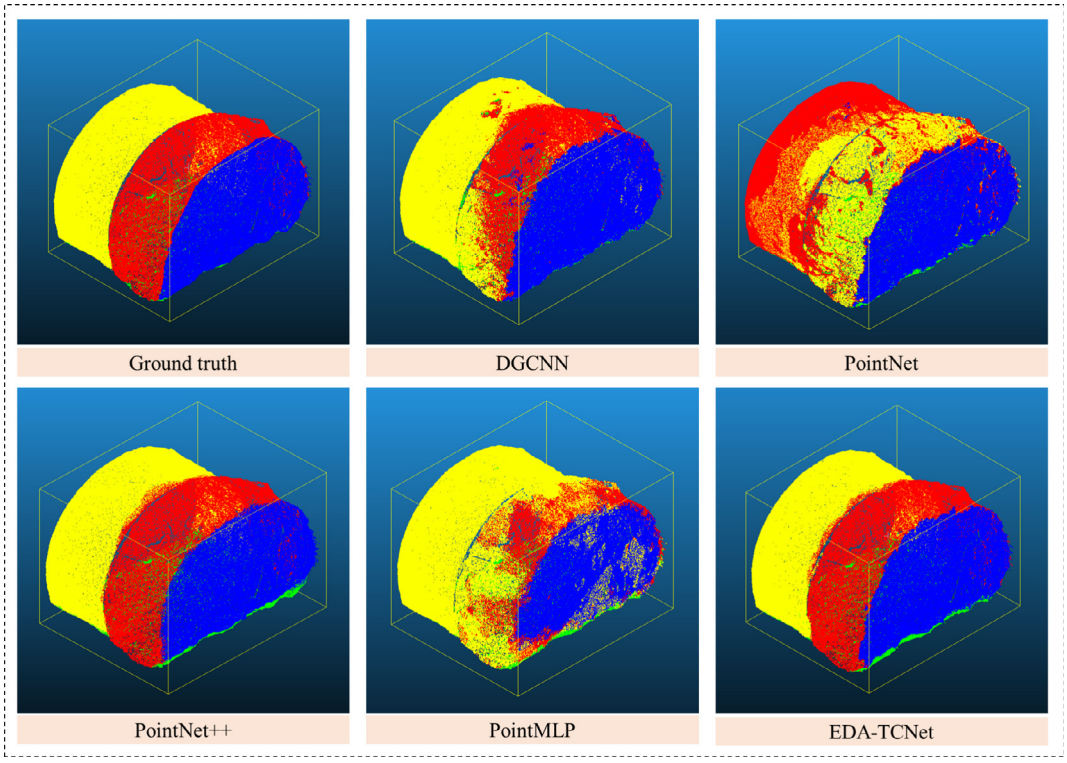

Fig. 11. Visual comparison between ground truth and predictions of the proposed model (back-side combined view).

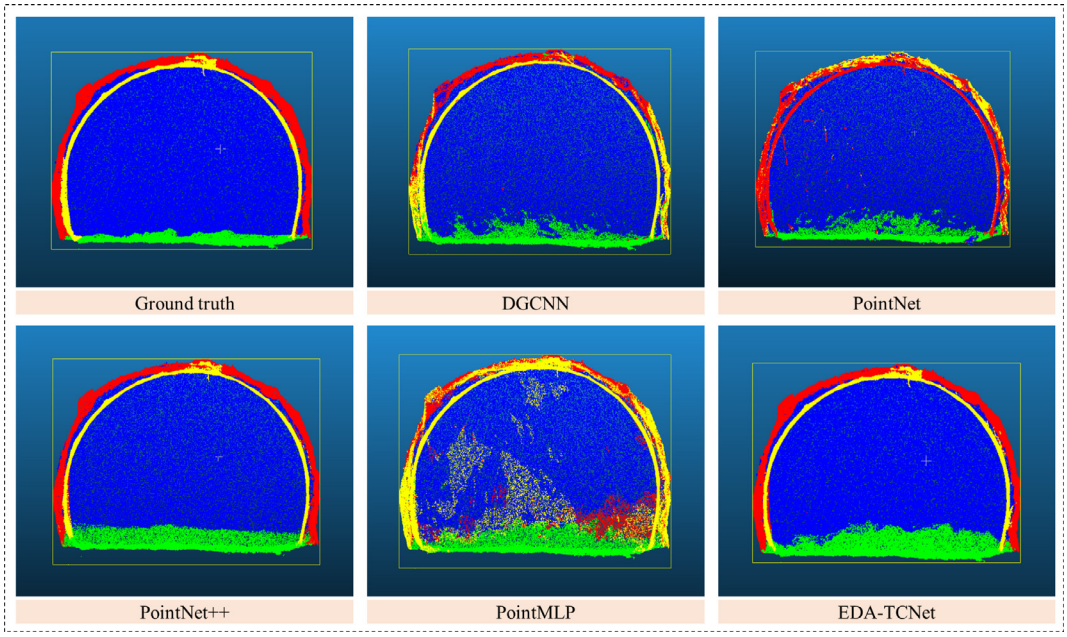

Fig. 12. Visual comparison between ground truth and predictions of the proposed model (front view).

These figures display the predictions from five models: DGCNN, PointNet, PointNet++, PointMLP, and EDA-TCNet, from three different perspectives: Back-side combined view, Front-side combined view, and Front view. Both PointNet++ and the proposed EDA-TCNet model achieved favorable prediction results, as evidenced by their visualizations.

The results demonstrate a high degree of consistency between the predictions and the ground truth, particularly within the internal boundary regions, where almost no points were misclassified. This indicates that the EDA-TCNet model performs exceptionally well in these areas. However, some deviations were observed in a few boundary regions. For instance, certain tunnel face areas were

Table 4
Comparison of model performance on the testing set.

Model categories	Metrics	Tunnel face	Ground surface	Initial support	Excavation profile	Inference time (s)
DGCNN	Recall	0.9199	0.9588	0.9441	0.7116	39
	F_1-score	0.9304	0.9023	0.9035	0.7994	–
	Precision	0.9413	0.8521	0.8663	0.9121	–
	IoU	0.8699	0.8220	0.8240	0.6659	–
	mIoU	0.7955	–	–	–	–
	OA	0.8858	–	–	–	–
PointNet	Recall	0.9411	0.9390	0.6505	0.7675	13
	F_1-score	0.9395	0.9175	0.7336	0.6538	–
	Precision	0.9380	0.8970	0.8412	0.5695	–
	IoU	0.8859	0.8476	0.5793	0.4857	–
	mIoU	0.6996	–	–	–	–
	OA	0.7808	–	–	–	–
PointNet++	Recall	0.9286	0.9717	0.9196	0.8909	14
	F_1-score	0.9295	0.9139	0.9445	0.8899	–
	Precision	0.9304	0.8627	0.9708	0.8888	–
	IoU	0.8683	0.8415	0.8949	0.8016	–
	mIoU	0.8516	–	–	–	–
	OA	0.9232	–	–	–	–
PointMLP	Recall	0.5896	0.9346	0.9961	0.1779	12
	F_1-score	0.7382	0.9312	0.7589	0.2900	–
	Precision	0.9871	0.9278	0.6130	0.7831	–
	IoU	0.5851	**0.8712**	0.6115	0.1696	–
	mIoU	0.5593	–	–	–	–
	OA	0.7168	–	–	–	–
EDA-TCNet	Recall	0.9219	0.9762	0.9468	0.9190	14
	F_1-score	0.9411	0.9283	0.9574	0.9207	–
	Precision	0.9611	0.8850	0.9683	0.9224	–
	IoU	**0.8887**	0.8663	**0.9183**	**0.8531**	–
	mIoU	**0.8816**	–	–	–	–
	OA	**0.9406**	–	–	–	–

misclassified as ground regions, highlighting potential areas for improvement in the model's boundary prediction accuracy. Overall, the model exhibits satisfactory performance on the testing set, effectively distinguishing between different semantic categories within the tunnel face construction area.

The experimental results on the testing set, as shown in Table 4, provide a comprehensive comparison of the segmentation performance among EDA-TCNet, DGCNN, PointNet, PointNet++, and PointMLP. Table 4 also gives the inference time of all models on the prediction set. Specifically, the inference time for DGCNN is 39 s, while the inference times for the other models range from 12 to 14 s. The results indicate that EDA-TCNet achieves the best performance across almost all evaluation metrics. Specifically, EDA-TCNet achieves an OA of 0.9406, representing improvements of 5.48%, 15.98%, 1.74%, and 22.38% compared to DGCNN, PointNet, PointNet++, and PointMLP, respectively. Additionally, EDA-TCNet achieves a mIoU of 0.8816, which is 8.61%, 18.20%, 3.00%, and 32.23% higher than the corresponding values for DGCNN, PointNet, PointNet++, and PointMLP. These results highlight the superior performance of EDA-TCNet in point cloud semantic segmentation tasks.

Among all the models, PointNet++ ranks second in overall performance, achieving an mIoU of 0.8516 and an OA of 0.9232. However, it struggles with boundary processing in the tunnel face and excavation profile categories. The segmentation capabilities of DGCNN, PointNet, and PointMLP are comparatively limited, with PointMLP exhibiting the lowest mIoU of 0.5593. Its performance is particularly inadequate in the tunnel face and excavation profile categories, with IoU values of 0.5851 and 0.1696, respectively. Furthermore, across all models, the IoU for the excavation profile category is consistently lower than that for other categories, highlighting the significant challenges posed by boundary complexity and feature ambiguity. Overall, EDA-TCNet demonstrates a clear advantage in capturing both global and detailed features. These strengths validate its practical potential for point cloud segmentation tasks in tunnel face construction areas.

Figure 13 presents the normalized confusion matrices for the models on the testing set, highlighting the notable advantages of EDA-TCNet (Fig. 13(e)). EDA-TCNet achieves higher classification accuracy than other models in the ground surface and excavation profile categories. In comparison, although PointNet++ (Fig. 13 (c)) performs better overall than PointNet, DGCNN, and

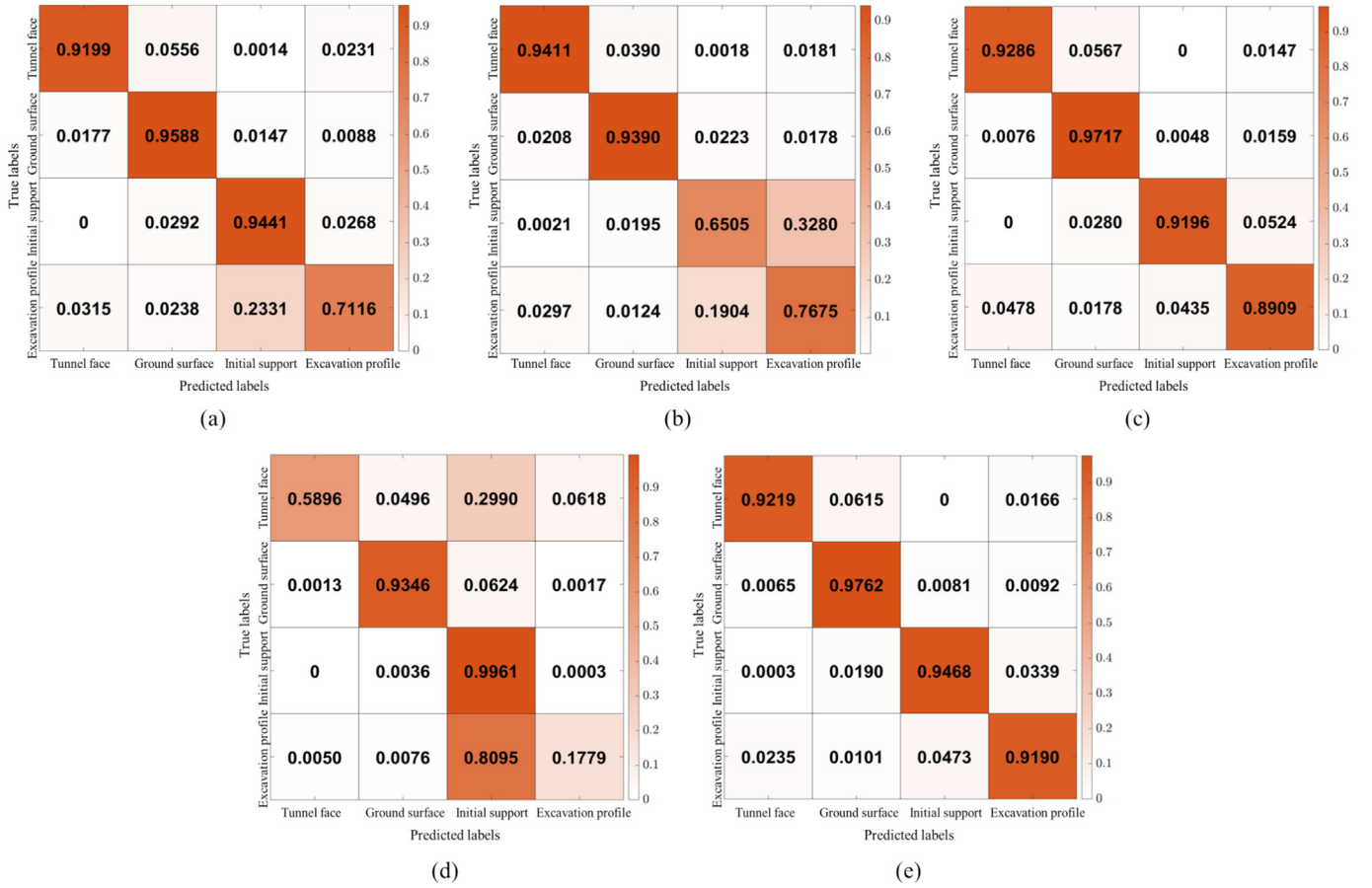

Fig. 13. Normalized confusion matrices of various models on the testing set. (a) DGCNN, (b) PointNet, (c) PointNet++, (d) PointMLP, and (e) EDA-TCNet.

PointMLP, its classification accuracy in the ground, initial support, and excavation profile categories remains lower than that of EDA-TCNet. PointNet (Fig. 13(b)) and DGCNN (Fig. 13(a)) show weaker overall performance, with particularly high misclassification rates in the excavation profile category. PointMLP has a high classification accuracy for initial support, but the accuracy of other categories is low, especially the excavation profile and the tunnel face (Fig. 13(d)). Overall, EDA-TCNet outperforms other models in classification accuracy, boundary processing, and generalization capability.

5 Discussion

The discussion section of this study provides a detailed analysis of the impact of different balancing coefficients (μ) on model performance, as shown in Table 5. The results indicate that when $\mu = 0.5$, the model achieves the best performance on the training set, with an mIoU of 0.8966 and an OA of 0.9565. However, the best validation set performance in terms of mIoU and OA is observed at $\mu = 0.5$ and $\mu = 0.3$, respectively, with values of 0.8937 and 0.9482. By adjusting the balancing coefficient, the OA on

Table 5
Effect of balancing coefficients on model training and validation performance.

μ	Training		Validation	
	OA	mIoU	OA	mIoU
0.1	**0.9568**	0.8946	0.9297	0.8606
0.3	0.9551	0.8919	**0.9482**	0.8871
0.5	0.9565	**0.8966**	0.9478	**0.8937**
0.7	0.9515	0.8837	0.9430	0.8843
0.9	0.9548	0.8911	0.9341	0.8662

Table 6
Effect of balancing coefficients on model testing performance.

μ	Testing				
	Recall	F_1-score	Precision	mIoU	OA
0.1	0.9224	0.9202	0.9199	0.8526	0.9168
0.3	**0.9438**	0.9390	**0.9351**	**0.8854**	**0.9479**
0.5	0.9410	**0.9369**	0.9342	0.8816	0.9406
0.7	0.9395	0.9333	0.9298	0.8752	0.9325
0.9	0.9253	0.9196	0.9168	0.8517	0.9236

the training set increased by 0.5%, and the mIoU increased by 1.29%. On the validation set, the OA improved by 1.85%, and the mIoU increased by 3.31%. These results suggest that adjusting μ within a specific range can effectively enhance model performance.

As μ increases, the OA and mIoU on the training set do not exhibit a monotonic trend but instead show some fluctuations. This indicates that overly low or high values of μ may lead to suboptimal feature learning for certain classes. On the validation set, the trends are more complex, with the OA peaking at $\mu = 0.3$ before slightly declining. This suggests that the optimal balancing coefficient for the validation set does not entirely align with the optimal value for the training set. Thus, it may be necessary to adjust μ based on the validation set's performance to achieve better generalization capability.

Table 6 illustrates the impact of different balancing coefficients (μ) on the model's performance on the testing set. The experimental results reveal that when $\mu = 0.3$, the model achieves the best values for most evaluation metrics, including Recall (0.9438), Precision (0.9351), mIoU (0.8854), and OA (0.9479), with a corresponding F_1-score of 0.9390. Notably, the F_1-score reaches its peak value of 0.9369 when $\mu = 0.5$. These results indicate that a lower μ value better addresses class imbalance issues on the testing set. Additionally, by adjusting the balancing coefficient, the improvement range from the lowest to the highest value for the five metrics is as follows: Recall (2.14%), F_1-score (1.73%), Precision (1.83%), mIoU (3.37%), and OA (3.11%). Among these, the most significant improvements are observed in mIoU and OA, highlighting the model's enhanced segmentation accuracy and overall performance under optimal balancing conditions.

Figure 14 presents the confusion matrices of the model on the prediction set under different values of the balancing coefficient μ. The results indicate that the model demonstrates good segmentation performance across all cases, though the classification accuracy for each category shows slight variations depending on the value of μ. By adjusting μ, the segmentation performance for specific regions can be optimized. For instance, when $\mu = 0.5$, the model achieves the best segmentation accuracy for the initial support category. At $\mu = 0.7$, the model excels in identifying and segmenting the excavation profile, while $\mu = 0.3$ yields optimal segmentation for the tunnel face region. Given that different tunnel projects may have varying segmentation requirements, flexibly adjusting μ allows the model to provide targeted optimization for specific areas.

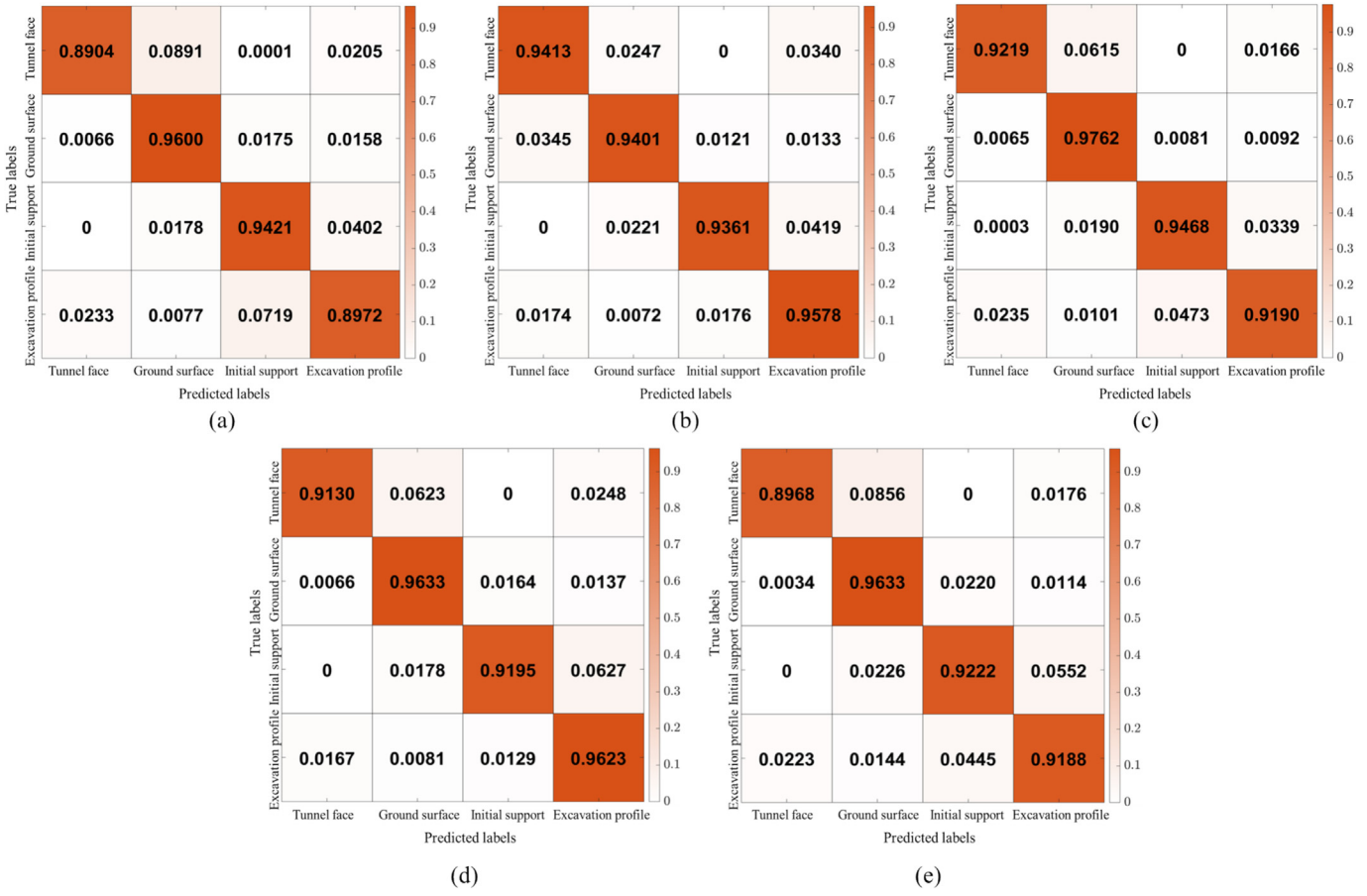

Fig. 14. Impact of balancing coefficients on the normalized confusion matrix for the testing set. (a) $\mu = 0.1$, (b) $\mu = 0.3$, (c) $\mu = 0.5$, (d) $\mu = 0.7$, and (e) $\mu = 0.9$.

Table 7
Performance of different loss functions on datasets.

Loss types	Training		Validation	
	mIoU	OA	mIoU	OA
Focal	0.8907	0.9559	0.8765	0.9401
Dice	0.8941	**0.9591**	0.8874	0.9409
CE	0.8966	0.9571	0.8713	0.9356
LDAM	0.8913	0.9537	0.8846	0.9432
CELDAM	**0.9020**	0.9568	**0.8937**	**0.9478**

To investigate the impact of different loss functions on model performance, we conducted a comparative study using several loss functions designed to address class imbalance: Focal Loss (Lin, 2017), Dice Loss (Li et al., 2019), CE Loss, LDAM Loss, and our proposed CELDAM Loss. The model's performance was evaluated across the training set and the validation set, with metrics including mIoU and OA. The results presented in Table 7 show that the best-performing loss functions vary depending on the dataset and evaluation metric. On the training dataset, CELDAM Loss achieves the highest mIoU (0.9020), while Dice Loss yields the best OA (0.9591). However, on the validation dataset, our proposed CELDAM Loss demonstrates the best performance for both mIoU (0.8937) and OA (0.9478). Furthermore, CELDAM outperforms standalone CE and LDAM Losses across almost all metrics, underscoring the effectiveness of its design. In conclusion, the results validate the efficacy of the proposed CELDAM Loss, particularly in handling class imbalance issues.

To explore potential further optimization of the model architecture and evaluate the impact of EDAM on model performance, we conducted experiments varying the quantity of EDAM modules. As shown in Table 8, the configuration with six EDAM modules (placed in all ESA and EFP layers) achieves the best performance. Specifically, when six EDAM modules are used, the model exhibits the highest mIoU (0.8937) and OA (0.9478) on the validation set, as well as the best mIoU (0.8816) and OA (0.9406) on the testing set, demonstrating the effectiveness of incorporating EDAM into every attention-sensitive layer.

Furthermore, the configuration with four EDAM modules (added to ESA_1–ESA_2 and EFP_1–EFP_2) performs better than the configuration with two EDAM modules (added to ESA_1 and EFP_1), indicating that increasing the number of EDAM modules enhances the model's segmentation accuracy and overall performance. However, when only two EDAM modules are used, the model's performance is slightly worse than when no EDAM modules are included. This counterintuitive result may be attributed to the insufficient utilization of EDAM's capabilities in this configuration, which could disrupt the balance of feature extraction across layers.

In conclusion, the results demonstrate that the strategic integration of EDAM into both the ESA and EFP layers can substantially enhance the model's performance. Notably, the comprehensive application of EDAM in all ESA and EFP layers yields the most significant improvements.

6 Conclusions

This paper proposes a novel point cloud semantic segmentation model named EDA-TCNet, aiming at improving segmentation accuracy in tunnel face construction areas. The core innovation of EDA-TCNet lies in the introduction of the 3D EDAM, which enhances the model's focus on critical features through a parallel channel and spatial attention mechanism. Additionally, to address data imbalance issues, a custom loss function, CELDAM, is designed. The application of EDA-TCNet in three ongoing tunnel projects in Northwest China, combined with comparisons against several classic models, demonstrates its superior accuracy. Based on the study, the following conclusions are drawn:

(1) EDA-TCNet achieves an mIoU of 0.8966 and an OA of 0.9565 on the training set, and an mIoU of 0.8937 and an OA of 0.9478 on the validation set. Compared to PointNet, PointNet++, DGCNN, and PointMLP, EDA-TCNet improves mIoU by 5.52%, 0.59%, 5.35%, and 2.50%, and OA by 2.53%, 0.12%, 2.25%, and 1.14%, respectively. These quantitative results indicate that EDA-TCNet demonstrates higher segmentation accuracy and stability during training and validation, showcasing significant advantages in feature extraction and classification capability.
(2) On the testing set, EDA-TCNet achieves an mIoU of 0.8816 and an OA of 0.9406, significantly outperforming PointNet (0.6996mIoU, 0.7808OA), PointNet++ (0.8516mIoU, 0.9232OA), DGCNN (0.7955mIoU, 0.8858OA), and PointMLP (0.5593mIoU, 0.7168OA). Additionally, visual com-

Table 8
Impact of EDAM quantity on model performance.

EDAM quantity	EDAM location	Training		Validation		Testing	
		mIoU	OA	mIoU	OA	mIoU	OA
0	–	0.8872	**0.9574**	0.8668	0.9362	0.8554	0.9222
2	ESA_1, EFP_1	0.8826	0.9518	0.8521	0.9233	0.8550	0.9200
4	ESA_1–ESA_2, EFP_1–EFP_2	0.8922	0.9569	0.8686	0.9351	0.8736	0.9322
6	ESA_1–ESA_3, EFP_1–EFP_3	**0.8966**	0.9565	**0.8937**	**0.9478**	**0.8816**	**0.9406**

parisons reveal that EDA-TCNet's predictions closely match ground truth in categories such as ground, initial support, and excavation profile, with minimal misclassifications within boundary regions. These results validate the superior generalization capability of EDA-TCNet and demonstrate its reliability in practical applications.

(3) Despite its outstanding performance in point cloud semantic segmentation, this study has limitations. First, the model is primarily designed for mountain tunnels constructed using the drilling-and-blasting method, with limited adaptability to other construction methods such as shield tunneling. Second, the diversity and scale of the dataset are constrained, as the samples are predominantly concentrated in relatively intact rock masses. Future work should involve collecting more point cloud data under varying geological conditions, including additional samples from tunnel faces of fractured rock masses, to enhance the model's generalization ability further. Moreover, there is still room for improvement in boundary prediction. We plan to explore specialized loss functions or post-processing methods to enhance boundary delineation accuracy. Additionally, future research should focus on optimizing the model architecture, and integrating advanced deep learning techniques to improve segmentation accuracy and adaptability, meeting broader engineering application demands.

Data availability

The data that used in this study are available on https://github.com/ROCKMASSPX/EDATCNet.

CRediT authorship contribution statement

Xin Peng: Writing – review & editing, Writing – original draft, Visualization, Validation, Methodology, Investigation, Conceptualization. **Mingnian Wang:** Writing – review & editing, Supervision, Resources, Project administration. **Bingxu Huang:** Validation, Data curation. **Honglin Shen:** Validation. **Hao Zhong:** Validation.

Declaration of competing interest

The authors declare that they have no known competing financial interests or personal relationships that could have appeared to influence the work reported in this paper.

Acknowledgement

This work was supported by the National Natural Science Foundation of China (Grant Nos. 52378411 and 51878567).

References

Attard, L., Debono, C. J., Valentino, G., & Di Castro, M. (2018). Tunnel inspection using photogrammetric techniques and image processing: A review. *Isprs Journal of Photogrammetry and Remote Sensing, 144*, 180–188.

Barton, N. (1988). Rock mass classification and tunnel reinforcement selection using the q-system.

Battulwar, R., Zare-Naghadehi, M., Emami, E., & Sattarvand, J. (2021). A state-of-the-art review of automated extraction of rock mass discontinuity characteristics using three-dimensional surface models. *Journal of Rock Mechanics and Geotechnical Engineering, 13*(4), 920–936.

Chen, J., Yang, T., Zhang, D., Huang, H., & Tian, Y. (2021a). Deep learning based classification of rock structure of tunnel face. *Geoscience Frontiers, 12*(1), 395–404.

Chen, J., Zhang, D., Huang, H., Shadabfar, M., Zhou, M., & Yang, T. (2020). Image-based segmentation and quantification of weak interlayers in rock tunnel face via deep learning. *Automation in Construction, 120*, 103371.

Chen, J., Zhou, M., Zhang, D., Huang, H., & Zhang, F. (2021b). Quantification of water inflow in rock tunnel faces via convolutional neural network approach. *Automation in Construction, 123*, 103526.

Cui, H., Li, J., Mao, Q., Hu, Q., Dong, C., & Tao, Y. (2024). STSD: A large-scale benchmark for semantic segmentation of subway tunnel point cloud. *Tunnelling and Underground Space Technology, 150*, 105829.

Daraei, A., & Zare, S. (2018). Prediction of overbreak depth in Ghalaje road tunnel using strength factor. *International Journal of Mining Science and Technology, 28*(4), 679–684.

Drews, T., Miernik, G., Anders, K., Höfle, B., Profe, J., Emmerich, A., & Bechstädt, T. (2018). Validation of fracture data recognition in rock masses by automated plane detection in 3D point clouds. *International Journal of Rock Mechanics and Mining Sciences, 109*, 19–31.

Fang, S., Xu, D., Zhao, Z., Song, Q., & Gui, W. (2024). Shotcrete flatness evaluation of initial linings based on vehicular LiDAR scanning. *Automation in Construction, 164*, 105475.

Foderà, G., Voza, A., Barovero, G., Tinti, F., & Boldini, D. (2020). Factors influencing overbreak volumes in drill-and-blast tunnel excavation. A statistical analysis applied to the case study of the Brenner Base Tunnel–BBT. *Tunnelling and Underground Space Technology, 105*, 103475.

García-Luna, R., Senent, S., Jurado-Piña, R., & Jimenez, R. (2019). Structure from Motion photogrammetry to characterize underground rock masses: Experiences from two real tunnels. *Tunnelling and Underground Space Technology, 83*, 262–273.

Gischig, V., Amann, F., Moore, J., Loew, S., Eisenbeiss, H., & Stempfhuber, W. (2011). Composite rock slope kinematics at the current Randa instability, Switzerland, based on remote sensing and numerical modeling. *Engineering Geology, 118*(1–2), 37–53.

Gong, J. F., Wang, W., Wang, F., Yang, C. X., & Yuan, Y. (2024). Statistics of China's railway tunnels by the end of 2023 and overview of tunnels of key new projects in 2023. *Tunnel Construction, 44*(2), 377–392 (in Chinese).

Grandio, J., Riveiro, B., Lamas, D., & Arias, P. (2023). Multimodal deep learning for point cloud panoptic segmentation of railway environments. *Automation in Construction, 150*, 104854.

Grandio, J., Riveiro, B., Soilán, M., & Arias, P. (2022). Point cloud semantic segmentation of complex railway environments using deep learning. *Automation in Construction, 141*, 104425.

Han, J.-Y., Guo, J., & Jiang, Y.-S. (2013). Monitoring tunnel deformations by means of multi-epoch dispersed 3D LiDAR point clouds: An improved approach. *Tunnelling and Underground Space Technology, 38*, 385–389.

He, C., & Wang, B. (2013). Research progress and development trends of highway tunnels in China. *Journal of Modern Transportation, 21*(4), 209–223.

Hong, Z., Tao, M., Cui, X., Wu, C., & Zhao, M. (2023). Experimental and numerical studies of the blast-induced overbreak and underbreak in underground roadways. *Underground Space, 8*, 61–79.

Ji, A., Zhang, L., Fan, H., Xue, X., & Dou, Y. (2023). Dual attention-based deep learning network for multi-class object semantic segmentation of tunnel point clouds. *Automation in Construction, 156*, 105131.

Jiang, M., Wu, Y., Zhao, T., Zhao, Z., & Lu, C. (2018). Pointsift: A sift-like network module for 3d point cloud semantic segmentation. *arXiv preprint arXiv:1807.00652*.

Kang, J., Chen, N., Li, M., Mao, S., Zhang, H., Fan, Y., & Liu, H. (2023). A point cloud segmentation method for dim and cluttered underground tunnel scenes based on the segment anything model. *Remote Sensing, 16*(1), 97.

Kemeny, J., & Post, R. (2003). Estimating three-dimensional rock discontinuity orientation from digital images of fracture traces. *Computers & Geosciences, 29*(1), 65–77.

Lee, J. S., Park, J., & Ryu, Y.-M. (2021). Semantic segmentation of bridge components based on hierarchical point cloud model. *Automation in Construction, 130*, 103847.

Li, X., Sun, X., Meng, Y., Liang, J., Wu, F., & Li, J. (2019). Dice loss for data-imbalanced NLP tasks. *arXiv preprint arXiv:1911.02855*.

Li, Y., Bu, R., Sun, M., Wu, W., Di, X., & Chen, B. (2018). Pointcnn: Convolution on x-transformed points. In *Advances in neural information processing systems* (pp. 31).

Lin, T. (2017). Focal Loss for Dense Object Detection. *arXiv preprint arXiv:1708.02002*.

Lin, W., Sheil, B., Zhang, P., Zhou, B., Wang, C., & Xie, X. (2024). Seg2Tunnel: A hierarchical point cloud dataset and benchmarks for segmentation of segmental tunnel linings. *Tunnelling and Underground Space Technology, 147*, 105735.

Ma, X., Qin, C., You, H., Ran, H., & Fu, Y. (2022). Rethinking network design and local geometry in point cloud: A simple residual MLP framework. *arXiv preprint arXiv:2202.07123*.

Mahtab, M., Rossler, K., Kalamaras, G., & Grasso, P. (1997). Assessment of geological overbreak for tunnel design and contractual claims. *International Journal of Rock Mechanics and Mining Sciences, 34*(3–4), 185, e181-185. e113.

Monsalve, J. J., Baggett, J., Bishop, R., & Ripepi, N. (2019). Application of laser scanning for rock mass characterization and discrete fracture network generation in an underground limestone mine. *International Journal of Mining Science and Technology, 29*(1), 131–137.

Nuttens, T., Stal, C., De Backer, H., Schotte, K., Van Bogaert, P., & De Wulf, A. (2014). Methodology for the ovalization monitoring of newly built circular train tunnels based on laser scanning: Liefkenshoek Rail Link (Belgium). *Automation in Construction, 43*, 1–9.

Peng, X., Wang, M., Huang, B., & Lin, P. (2024). Efficient automated method for characterizing discontinuities in tunnel face rock mass point clouds. *Tunnelling and Underground Space Technology, 154*, 106117.

Phan, A. V., Le Nguyen, M., Nguyen, Y. L. H., & Bui, L. T. (2018). Dgcnn: A convolutional neural network over large-scale labeled graphs. *Neural Networks, 108*, 533–543.

Priest, S. D. (1993). Discontinuity analysis for rock engineering. Dordrecht: Springer, Netherlands.

Qi, C. R., Su, H., Mo, K., & Guibas, L. J. (2017a). Pointnet: Deep learning on point sets for 3d classification and segmentation. In *Proceedings of the IEEE conference on computer vision and pattern recognition* (pp. 652–660).

Qi, C. R., Yi, L., Su, H., & Guibas, L. J. (2017b). Pointnet++: Deep hierarchical feature learning on point sets in a metric space. In *Advances in Neural Information Processing Systems* (pp. 30).

Roca-Pardiñas, J., Argüelles-Fraga, R., de Asís López, F., & Ordóñez, C. (2014). Analysis of the influence of range and angle of incidence of terrestrial laser scanning measurements on tunnel inspection. *Tunnelling and Underground Space Technology, 43*, 133–139.

Singh, S. K., Banerjee, B. P., Lato, M. J., Sammut, C., & Raval, S. (2022). Automated rock mass discontinuity set characterisation using amplitude and phase decomposition of point cloud data. *International Journal of Rock Mechanics and Mining Sciences, 152*, 105072.

Singh, S. K., Banerjee, B. P., & Raval, S. (2023). A review of laser scanning for geological and geotechnical applications in underground mining. *International Journal of Mining Science and Technology, 33*(2), 133–154.

Singh, S. K., Raval, S., & Banerjee, B. P. (2021). Automated structural discontinuity mapping in a rock face occluded by vegetation using mobile laser scanning. *Engineering Geology, 285*, 106040.

Singh, S. P., & Xavier, P. (2005). Causes, impact and control of overbreak in underground excavations. *Tunnelling and Underground Space Technology, 20*(1), 63–71.

Soilán, M., Nóvoa, A., Sánchez-Rodríguez, A., Riveiro, B., & Arias, P. (2020). Semantic segmentation of point clouds with pointnet and kpconv architectures applied to railway tunnels. *ISPRS Annals of the Photogrammetry, Remote Sensing and Spatial Information Sciences, 2*, 281–288.

Sun, X., He, L., Jiang, H., Li, R., Mao, W., Zhang, D., Majeed, Y., Andriyanov, N., Soloviev, V., & Fu, L. (2024). Morphological estimation of primary branch length of individual apple trees during the deciduous period in modern orchard based on PointNet++. *Computers and Electronics in Agriculture, 220*, 108873.

Wang, W., Yu, R., Huang, Q., & Neumann, U. (2018). Sgpn: Similarity group proposal network for 3d point cloud instance segmentation. *Proceedings of the IEEE conference on computer vision and pattern recognition*.

Woo, S., Park, J., Lee, J.-Y., & Kweon, I. S. (2018). Cbam: Convolutional block attention module. *Proceedings of the European conference on computer vision (ECCV)*.

Xie, Y., Tian, J., & Zhu, X. X. (2020). Linking points with labels in 3D: A review of point cloud semantic segmentation. *IEEE Geoscience and remote sensing magazine, 8*(4), 38–59.

Yang, X., Lu, B., Jing, Q., Li, Y., & Zhou, Y. (2023). Macrotexture deterioration for micromilled tunnel concrete pavement using 3D laser data. *Measurement Science and Technology, 34*(6), 065001.

Yin, C., Wang, B., Gan, V. J., Wang, M., & Cheng, J. C. (2021). Automated semantic segmentation of industrial point clouds using ResPointNet++. *Automation in Construction, 130*, 103874.

Zeng, Y., & Wang, Z. (2014). A policy analysis on challenges and opportunities of population/household aging in China. *Journal of Population Ageing, 7*(4), 255–281.

Zhang, L., & Wang, H. (2021). A novel segmentation method for cervical vertebrae based on PointNet++ and converge segmentation. *Computer Methods and Programs in Biomedicine, 200*, 105798.

Zhang, L., Wei, Z., Xiao, Z., Ji, A., & Wu, B. (2024). Dual hierarchical attention-enhanced transfer learning for semantic segmentation of point clouds in building scene understanding. *Automation in Construction, 168*, 105799.

Zhang, Z., Ji, A., Wang, K., & Zhang, L. (2022). UnrollingNet: An attention-based deep learning approach for the segmentation of large-scale point clouds of tunnels. *Automation in Construction, 142*, 104456.

Zhang, Z., Ji, A., Zhang, L., Xu, Y., & Zhou, Q. (2023). Deep learning for large-scale point cloud segmentation in tunnels considering causal inference. *Automation in Construction, 152*, 104915.

Zhao, H., Jiang, L., Jia, J., Torr, P. H., & Koltun, V. (2021). Point transformer. *Proceedings of the IEEE/CVF international conference on computer vision*.

Zhou, J.-W., Chen, J.-L., & Li, H.-B. (2024). An optimized fuzzy K-means clustering method for automated rock discontinuities extraction from point clouds. *International Journal of Rock Mechanics and Mining Sciences, 173*, 105627.

Zhou, Y., Ji, A., Zhang, L., & Xue, X. (2023). Attention-enhanced sampling point cloud network (ASPCNet) for efficient 3D tunnel semantic segmentation. *Automation in Construction, 146*, 104667.

Zhu, H., Yan, J., & Liang, W. (2019). Challenges and development prospects of ultra-long and ultra-deep mountain tunnels. *Engineering, 5*(3), 384–392.